

Systematic evaluation of variability detection methods for eROSITA

Johannes Buchner^{1*}, Thomas Boller¹, David Bogensberger¹, Adam Malyali¹, Kirpal Nandra¹, Joern Wilms², Tom Dwelly¹, and Teng Liu¹

¹ Max Planck Institute for Extraterrestrial Physics, Giessenbachstrasse, 85741 Garching, Germany

² Dr. Karl Remeis-Observatory and Erlangen Centre for Astroparticle Physics, Friedrich-Alexander-Universität Erlangen-Nürnberg, Sternwartstr. 7, 96049 Bamberg, Germany

-Received date / Accepted date

ABSTRACT

The reliability of detecting source variability in sparsely and irregularly sampled X-ray light curves is investigated. This is motivated by the unprecedented survey capabilities of eROSITA onboard SRG, providing light curves for many thousand sources in its final-depth equatorial deep field survey. Four methods for detecting variability are evaluated: excess variance, amplitude maximum deviations, Bayesian blocks and a new Bayesian formulation of the excess variance. We judge the false detection rate of variability based on simulated Poisson light curves of constant sources, and calibrate significance thresholds. Simulations with flares injected favour the amplitude maximum deviation as most sensitive at low false detections. Simulations with white and red stochastic source variability favour Bayesian methods. The results are applicable also for the million sources expected in eROSITA's all-sky survey.

1. Introduction

The variability of astrophysical sources is a powerful diagnostic to differentiate between different physical models even when those models predict similar spectral energy distributions. Variability studies have enriched the zoo of astrophysical phenomena with new mysteries, including in recent years for example fast radio bursts (Lorimer et al. 2007; Petroff et al. 2019), ultra-luminous X-ray sources (e.g., Bachetti et al. 2014; Liu et al. 2013) and quasi-periodic eruptions (Miniutti et al. 2019). In high-energy astrophysics, the search for transient phenomena has a long history with gamma-ray bursts (Klebesadel et al. 1973; Gehrels & Mészáros 2012), for example. Missions such as MAXI (Matsuoka et al. 2009), Rossi X-ray Timing Explorer (Swank 2006) and Swift (Gehrels et al. 2004) were explicitly designed to characterize the variable X-ray sky. However, these missions are sensitive only to the brightest objects (typically fewer than one hundred variability triggers per year). This situation has changed with the launch of the eROSITA telescope on-board SRG (Predehl et al. 2021), and its all-sky monitoring every 6 months in the first 4 years. Because eROSITA scans the X-ray sky rapidly over large areas down to faint fluxes, it has the potential to reveal a myriad of diverse variable and transient phenomena. Preliminary analysis of the first, most extreme events revealed gamma-ray burst afterglows (Weber 2020), super-soft emission from a classical nova (Ducci et al. 2020), flares in millisecond pulsars (Koenig et al. 2020), flares of unknown origin (Wilms et al. 2020) and new types of tidal disruption events (Malyali et al. 2021). These phenomena exhibit different variability behaviour (e.g., flares or red noise). To fully exploit the eROSITA dataset we require robust and well characterized techniques to

identify, classify and characterize the variability properties of each detected X-ray source.

Identifying source variability in the X-rays is no small task. In the recent, large-scale optical photometric surveys (Gaia, Zwicky Transient Factory, Optical Gravitational Lensing Experiment, etc.), systematics typically dominate measurement uncertainties, requiring a machine learning classifier to postprocess various classical light curve summary statistics (Debosscher et al. 2007; Kim et al. 2011; Palaversa et al. 2013; Masci et al. 2014; Armstrong et al. 2016; Holl et al. 2018; Heinze et al. 2018; Jayasinghe et al. 2019; van Roestel et al. 2021). In contrast, for repeated X-ray surveys where most X-ray sources are found near the detection limit, statistical (Poisson) uncertainties are dominant. In this regime, methods such as fractional variance (Edelson et al. 1990), excess variance (Nandra et al. 1997) and Bayesian blocks (Scargle et al. 2013) have been proposed. However, their application has typically been limited to a handful of light curves at a time. De Luca et al. (2021) investigated variable objects of the archival XMM-Newton X-ray sky with Bayesian blocks and light curve summary statistics. eROSITA detected almost a million point sources already in its first all-sky survey (eRASS1), and a new all-sky survey with similar characteristics is conducted every 0.5 years. With this many sources, the calibration of the instrument and detection methods becomes important to avoiding both false positives and false negatives in large numbers. Additionally, eROSITA's scanning pattern imprints strong temporal modulations of the effective instrument sensitivity at any particular sky location. To summarise, any useful method must consistently distinguish Poisson and sensitivity fluctuations from variations intrinsic to the astrophysical source. For these reasons, we have examined the performance of commonly used variability

* johannes.buchner.acad@gmx.com

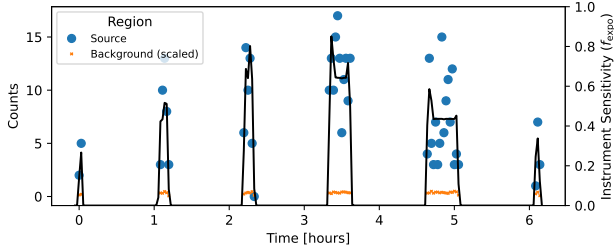


Fig. 1. Example counts of the 10th brightest eFEDS source. The markers indicate the number of counts from a single *eROSITA* telescope module in 100s time bins, recorded over a six hour period. The black curve shows the sensitivity to the source position over time.

analysis methods, together with a novel Bayesian approach, within the eROSITA regime.

This paper investigates the reliability and sensitivity of various variability detection methods, based on a pilot *eROSITA* survey over a extra-galactic 140 square degrees field. Its characteristics, such as exposure depth, are similar to the final stacked eight-year all-sky surveys. Classes of variable sources expected include flaring X-ray stars and variable active galactic nuclei. The properties of that data set is presented in §2, including how counts are extracted in time bins. Various ways for constructing light curves (§3.1) and visualising them (§3.2) are discussed. These light curves form the foundation for the considered variability detection methods, which are presented in detail in §3.3. Section 3.4 explains our methodology for evaluate and compare the methods, based on extensive numerical simulations (§3.5). The results section presents the calibrations needed for reliable use of the methods (§4.1) and how sensitive they are to various types of variability (§4.2). We conclude with discussing in §5 the advantages of a method newly developed in this work, Bayesian excess variance, and its future use for *eROSITA* and beyond.

2. Data

The eROSITA Final Equatorial-Depth Survey (eFEDS) field was observed with *eROSITA* in November 2019. The source catalog paper (Brunner et al. 2021) presents the observations, eROSITA analysis software and data treatment. Survey aspects that are important for investigating source variability are highlighted in this section. The depth expected after completion of all eROSITA all-sky survey scans was reached and slightly exceeded in the eFEDS field. eFEDS consists of four adjacent, approximately rectangular areas aligned with the Ecliptic coordinate grid, which were covered from Ecliptic east to west by a sequence of linear scans going from Ecliptic north to south and back. The typical scanning speed was 13.15"/s (Brunner et al. 2021). Because the field of view (FoV) of *eROSITA* is about ten times larger than the distance between scans, each source was covered multiple times. The resulting cadence is such that sources were visible continuously for several minutes, and revisited approximately every hour. The black curve of Figure 1 illustrates this strongly variable instrument sensitivity over time for a typical source. This illustrates the difference

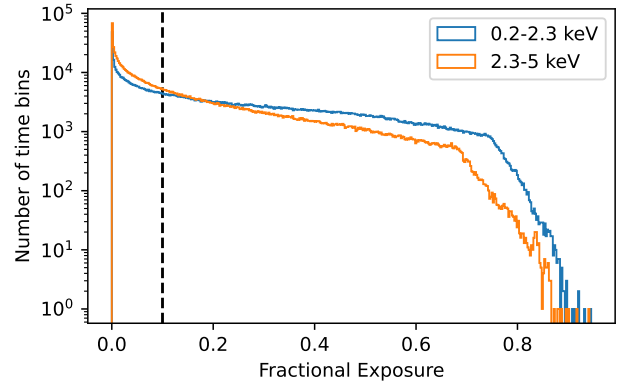


Fig. 2. Distribution of fractional exposure (f_{expo}) values for all light curve time bins.

between eROSITA survey light curves and those of typical pointed observations, where the instrument sensitivity is nearly constant. Therefore different analysis methods are required. In eFEDS, 27910 point sources were detected (Brunner et al. 2021) in the 0.2-2.3 keV band. These form the main eFEDS sample, which is also the basis of this paper.

For all 27910 sources, a spectrum and light curve was extracted. The procedure is described in detail in Liu et al. (2021). Source counts are extracted from a circular aperture of radius $\approx 20 - 40''$ (increasing with source counts). A representative local background is extracted from an annular region, also centred at the source position. The inner and outer radii of the annulus are scaled to be 5 and 25 times larger than the source radius, which yields a background to source area ratio of $r' \approx 200$. Because most *eROSITA* observations are made in scanning mode, these extraction regions are defined in terms of sky coordinates (rather than on some instrumental coordinate system). Neighbouring sources are masked from the source and background regions before extraction, and finally the light curves from the seven telescope modules are summed (see Liu et al. 2021). Figure 1 shows an example of counts extracted over time for a bright source, with the background counts scaled according to the area ratio. The count statistics are low and therefore in the Poisson regime.

Light curves are extracted in three bands. Their energy ranges are 0.2-5 (full band, band 0), 0.2-2.3 (soft band, band 1), and 2.3-5 keV (hard band, band 2). Here, we focus primarily on the soft, and secondarily on the properties of the hard band light curves. Because of *eROSITA*'s relatively soft X-ray response, the full band is dominated by, and nearly identical to, the soft band for most detected sources.

Light curves with time bins of 100s were constructed using `srctool`¹ (Brunner et al. 2021, version eSASSUsers_201009). This binning choice balances samples times during the survey track as well as revisits. The effective sensitivity of *eROSITA* to an astrophysical source varies with time, as the source moves through the FoV of the telescope modules, and becomes zero in time bins while the source is outside the FoV. The dimensionless fractional exposure (f_{expo}) parameter (range 0 to 1) computed by `srctool`, is an

¹ https://erosita.mpe.mpg.de/eR0doc/tasks/srctool_doc.html

estimate of the effective sensitivity of the instrument within a time bin to the source in question. The computation of f_{expo} for each bin of the light curve is carried out by integrating the instantaneous effective response of the instrument within the bin, on a time grid comparable to the instrumental integration time (Delta $t=50$ ms). The computation of f_{expo} takes into account the geometry of the source extraction aperture, the telescope attitude, off-axis vignetting, energy- and position-dependent point spread function (PSF), good time intervals, instrument dead time, and the location any bad pixels, and is carried out independently for each of the seven telescope modules. An effective spectral index of $\Gamma = 1.7$ is assumed when weighting the energy-dependent components of the instrument response model (vignetting, PSF) across broad energy bins. We normalize f_{expo} relative to the response expected for an on-axis point source observed with all telescope modules, assuming no extraction aperture losses. The black curve of Figure 1 gives an example of the f_{expo} windowing for an arbitrarily chosen source in eFEDS, decreasing when the source is at the border of the field of view. Figure 2 shows the f_{expo} of all time bins for sources in the eFEDS field. Because the current understanding of the *eROSITA* vignetting function is somewhat uncertain at large off-axis angles, we only consider time bins exposed to $f_{\text{expo}} > 0.1$. This cut tends to segment the light curves into disjoint intervals that are filled with meaningful data. As the reflectivity of the *eROSITA* optics reduces at higher energies and large grazing angles, the hard band has a smaller effective field of view and systematically lower f_{expo} values (see Figure 2). Unless otherwise stated, the remainder of this paper assumes that f_{expo} represents the relative sensitivity of the instrument correctly.

The cadences effectively sampled by the light curves are summarized in Figure 3. The top panel illustrates that sources are typically observed over a span of four to seven hours. During this time, the light curves exhibit several gaps (see Figure 1), during which other parts of the field were scanned. Typically, there are four to twelve blocks of contiguous observations (middle panel of Figure 3), lasting not more than a few minutes each. This results in two effective cadences: consecutive exposures lasting a few minutes and revisits on hour time-scales.

For each time bin the observed source counts S and background counts B are listed. Figure 4 presents histograms of these counts, for the soft (blue) and hard (orange) band. For most time bins, the number of counts is in the single digits, contributed by sources near the detection threshold. *eROSITA* is most sensitive in the soft band, which typically shows more counts (up to 100 cts/bin), approximately 20 times higher than the maximum seen in the hard band. The expected number of background counts in each time bin is typically below 1. Light curves are presented in Boller et al. (2021), and significantly variable sources are identified. This focus of this work is to investigate methods to determine whether sources are significantly variable.

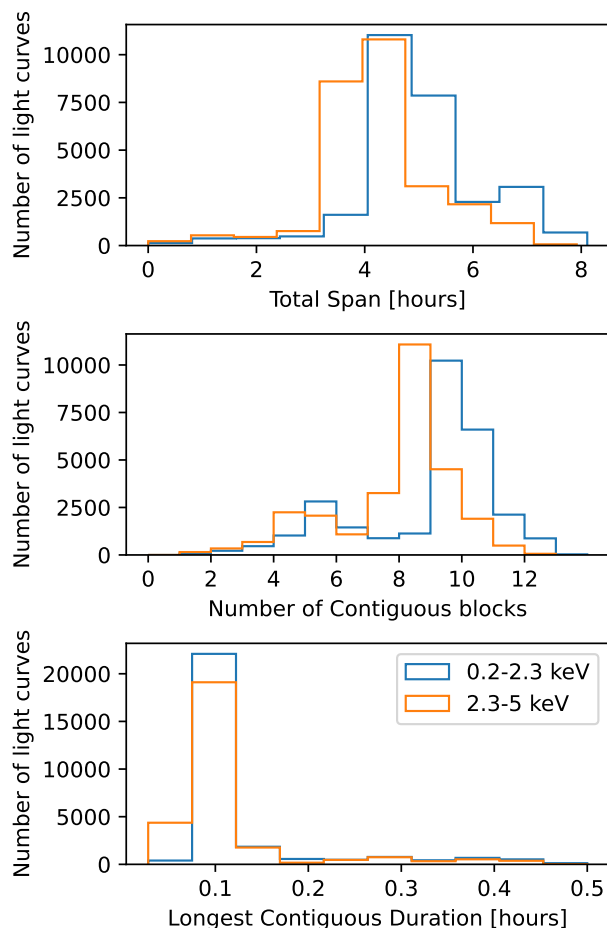


Fig. 3. Light curve cadence summary statistics. The *top panel* shows the time between first and last exposed time bins for each light curve, with typical values of four to seven hours. As Figure 1 illustrates, the lightcurves are segmented into blocks. The *middle panel* counts the number of blocks, which range from four to twelve. The *bottom panel* shows the duration of the longest block for each light curve, which is typically last only a few minutes.

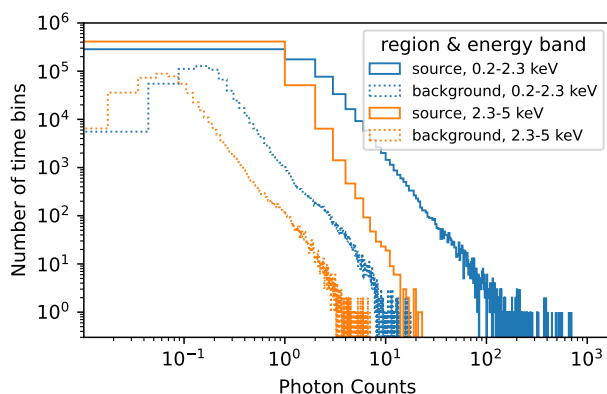


Fig. 4. Source and background photon count distribution in the soft and hard bands. The background counts are scaled by the source to background area ratio.

3. Methods

The counts observed in a time bin t can be expressed as a Poisson process, which integrates the band count rate R , dampened by the efficiency f_{expo} within the time interval Δt . For the background region and as-

suming f_{expo} is constant within the time bin, this can be written as

$$B \sim \text{Poisson}(R_B \times f_{\text{expo}} \times \Delta t) \quad (1)$$

where $C \sim \text{Poisson}(\lambda)$ means “Counts C is a Poisson random variable with a mean of λ ”. The total counts in the source region, S , contain contributions from the source, with count rate R_S and background:

$$S \sim \text{Poisson}((R_S + R_B \times r) \times f_{\text{expo}} \times \Delta t) \quad (2)$$

The background rate R_B is scaled by the area ratio of source and background extraction regions, r , with values near 1% being typical. The unknowns are R_B , the background count rate and R_S , the net (without background) source count rate. Typical values for $R_S/(R_B \times r)$ are 8 for the soft band and 1 for the hard band.

3.1. Methods to infer the source count rate per-bin

In the following, we present two approaches for inferring the net count rate R_S in each time bin.

3.1.1. Classic per-bin source rate estimates

The classic point estimator for the net source count rate R_S is:

$$\hat{R}_S = \frac{S - B \times r}{f_{\text{expo}} \times \Delta t} \quad (3)$$

Here, the background count rate in the background region is estimated with:

$$\hat{R}_B = \frac{B}{f_{\text{expo}} \times \Delta t} \quad (4)$$

The uncertainty in the net source count rate $\hat{R}_S(t)$ is estimated as:

$$\hat{\sigma}(R_S)(t) = \frac{\sqrt{\hat{\sigma}(S)(t)^2 + \hat{\sigma}(B)(t)^2 \times r}}{f_{\text{expo}}(t) \times \Delta t} \quad (5)$$

Here, $\hat{\sigma}(C)$ (with C either S or B) is the uncertainty of the expected number of counts, given the observed counts C . One possibility is to use the simple $\hat{\sigma}(C) = \sqrt{C}$ estimator. However, in the low count regime, the uncertainties are then severely under-estimated (for example, when $S = 0$). These leads to a strong count-dependent behaviour of any method that ingests these uncertainties.

Confidence intervals for the Poisson processes have been studied extensively in the X-ray and gamma-ray astronomy literature (e.g., Gehrels 1986; Kraft et al. 1991). They are asymmetric in general for realistic settings, and thus cannot be readily propagated in equation 5. We adopt the upper confidence interval formula $\hat{\sigma}(C) = \sqrt{C + 0.75} + 1$ from (Gehrels 1986), and use it also as a lower confidence interval, instead of the formula $\hat{\sigma}(C) = \sqrt{C - 0.25}$. This conservative choice tends to enlarge the error bars, and thus makes the data appear less powerful than they actually are. An alternative that is being considered for future releases of srctool are maximum likelihood-derived confidence intervals found by numerically exploring profile likelihoods (Barlow 2003).

3.1.2. Bayesian per-bin source rate estimates

A drawback of the estimates above is the Gaussianity error propagation. In the low-count regime, the Poisson uncertainties become asymmetric. We adopt the approach of Knoetig (2014) to propagate the uncertainties in a Bayesian framework.

Firstly, the unknown background count rate $R_B(t)$ only depends on known quantities in eq. 1. The Poisson process likelihood, $\text{Poisson}(C|\lambda) = \lambda^k \times e^{-\lambda}/k!$, can be combined with a flat, improper prior on the expected count rate $\lambda = R_B \times f_{\text{expo}}$, to define a posterior that can be numerically inverted using the inverse incomplete Gamma function Γ^{-1} (see also Cameron 2011). Specifically, the q -th quantile of the posterior probability distribution of $R_B(t)$ can be derived as $\Gamma^{-1}(B + 1, q) \times r / f_{\text{expo}}$. The same approach cannot be applied to R_S , because it depends on the values of S and $R_B(t)$ (eq. 2). We thus compute the marginalised likelihood function of the source rate R_S as:

$$P(S|R_S) = \int_{R_B} P(B|R_B) \times P(S|R_S + R_B) \times \pi(R_B) \quad (6)$$

$$= \int_0^1 P(S|R_S + \Gamma^{-1}(B + 1, q) \times r) dq \quad (7)$$

In practice, equation 6 is evaluated by numerically integrating over q in a grid (see Knoetig 2014, for an alternative method).

The goal is then to place constraints on R_S using the likelihood function $P(S|R_S)$. Evaluating a grid over $R_S(t)$ over a reasonable range (logarithmically between 0.01 and 100 cts/s) explores the likelihood function of eq. 6. If the grid points are interpreted to be equally probable a priori, quantiles (median, 1 σ -equivalents) can then be read off the normalised cumulative of $P(S|R_S)$ grid values, and form Bayesian alternatives for $\hat{R}_S(t)$ and $\hat{\sigma}$. A different approach to the priors on R_S is explored below in section 3.3.4.

3.2. Visualisations

The per-bin estimates defined above provide the possibility to plot time series of inferred source count rates (a light curve). An example (simulated) light curve is shown in Figure 5, with both Classical and Bayesian error bar estimates. The classical confidence intervals are symmetric and sometimes include negative count rates. The Bayesian estimates are asymmetric and always positive.

Some forms of variability can then be judged by identifying if the count rates are consistent over time. In Figure 5, one may identify a major flare near $t = 4000$ s, and perhaps two minor ones. One shortcoming of this approach is that the judgment by eye is subjective and difficult to reproduce. The Poisson fluctuations are also unintuitive (there was only one real flare injected in this simulated time series). Nevertheless, it can be insightful to try to understand what various methods “see”, and try to understand what likely triggered a statistical test. They are also useful for judging the plausibility of the data under current calibration. For example, if the fractional exposure f_{expo} is mis-estimated at large off-axis angles, the count rates are enhanced or reduced while the source

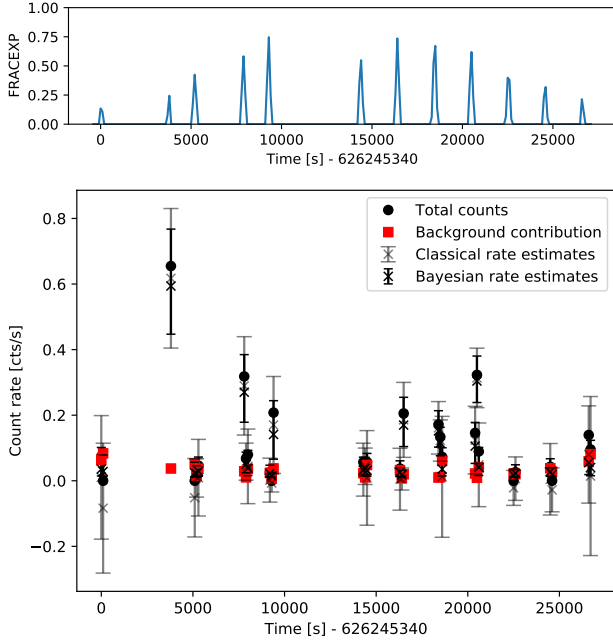


Fig. 5. Visualisations. *Top panel:* The fractional exposure over time for an example source with 10 passes. *Bottom panel:* Light curve of a simulated source with constant count rate and a bright flare. Black circles show the total counts without background subtraction, red points show the expected background count rates in the source region (eq. 4). Gray error bars show Classical net source count rate estimates (eq. 3 and 5). Black error bars show Bayesian net source count rate posterior distributions, represented visually with 10%, 50% and 90% quantiles under a log-uniform prior (eq. 7).

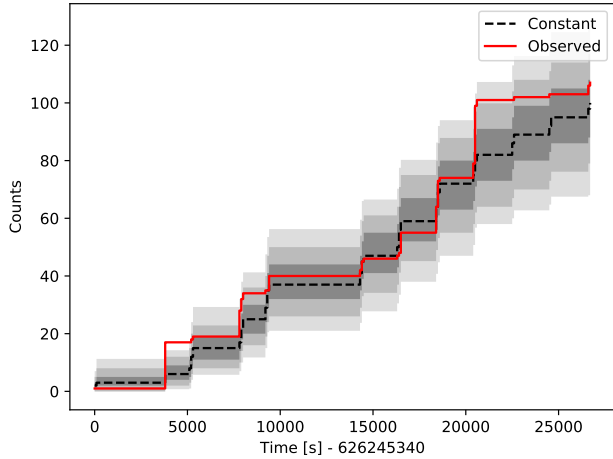


Fig. 6. Cumulative count visualisation. The red curve are the observed cumulative counts over time. The expectation of a constant source is indicated as a dashed curve and gray intervals corresponding to 1, 2 and 3 σ .

enters and leaves the field-of-view. Such systematic over- or under-corrections can become visible as U or inverse U shaped light curves.

The binning of the time series also influences the visualisation. Large time bins may average out short-term variability. Small time bins may contain too few counts and thus large uncertainties. The accumulation of nearby data points is difficult to do by eye. However, this can be important, as variations are typically correlated on short time-scales.

Cumulative counts address some of these limitations. Figure 6 plots the cumulative counts in the source region, S , over time, as a red curve. In the last time bin, all counts are noted. For judging whether this light curve is variable, we generate Poisson counts for 1000 simulated time series assuming a constant source, following eq. 2. For this, the classically inferred source and background count rates are assumed. The generated counts are shown in Figure 6, with the mean as dashed black curve and intervals corresponding to 1, 2 and 3 σ as gray shadings. For this source, we see that near 4000s, the red curve departs above the 3 σ range, indicating an excess of counts at that time (consistent with 5). At the other times, the variations are within the 3 σ intervals.

The benefit of the cumulative count plot is that it is independent of any binning. It stacks the information of neighbouring time bins. Instead of modifying the data through background subtraction, the data are fixed. A drawback is that time intervals cannot be investigated in isolation, as all time bins are correlated to the time bins before. Furthermore, these visualisations are not rigorous statistical variability tests, as the data will lie outside the 3 σ regions occasionally, given enough time bins.

3.3. Methods for variability detection

In this section, methods for detecting and quantifying variability are contrasted. In eFEDS, the time series are sparsely sampled (see §2). Within a total length of only a few hours, each source is typically continuously observed for a few minutes, about $N \sim 20$ times (less often at the edges of the field). In this setting, we test several methods for their ability to detect variability, and quantify how sensitive they are to different types of variability.

3.3.1. Amplitude Maximum Deviation methods

The simplest definition of variability is that two measured source rates disagree with each other. This implies that the source has changed.

Assuming Gaussian error propagation, Boller et al. (2016) defined the Amplitude Maximum Deviation ($ampl_max$) as the tension between the most extreme points:

$$AMPL_MAX = (\hat{R}_S(t_{max}) - \hat{\sigma}(R_S)(t_{max})) - (\hat{R}_S(t_{min}) + \hat{\sigma}(R_S)(t_{min})) \quad (8)$$

where t_{min} and t_{max} are the time bins with the lowest and highest \hat{R} source rate estimate. The $ampl_max$ is the distance between the lower error bar of the maximum value to the upper error bar of the minimum value. By comparing the span to the error bars, the significance can be quantified in units of standard deviations (i.e., as a z-score):

$$AMPL_SIG = \frac{AMPL_MAX}{\sqrt{\hat{\sigma}(R_S)(t_{max})^2 + \hat{\sigma}(R_S)(t_{min})^2}} \quad (9)$$

This method is conservative, as it considers the error bars twice. A drawback of this method is the assumption that the errors are Gaussian. With the asymmetric Poisson errors derived in section 3.1.2, one

could define an analogous Bayesian AMPL_MAX and AMPL_SIG by modifying eq. 9 to use the Bayesian quantile uncertainties instead of $\hat{\sigma}(R)$. Such a modified method was considered for the simulations performed in this paper. However, it yielded comparable efficiency in detecting variability. This is probably because this method is limited primarily by considering only the two extreme data points, rather than by a refinement of the error bars.

The Amplitude Maximum Deviation quantifies both the size of the effect (eq. 8) and its statistical significance (eq. 9). Because only the two most extreme data points are considered, it is thus insensitive to the variations in the other values.

3.3.2. Bayesian blocks

The Bayesian blocks algorithm Scargle et al. (2013) identifies in a sequence of measurement points where the rate changed. This adaptive binning technique automatically segments a light curve into blocks of constant rates separated by change points. The criterion to decide the number and location of the change points is based on Bayesian model comparison. For a certain class of likelihood functions, Scargle et al. (2013) derived analytic recursive formulas which quickly construct the globally optimal segmentation. Bayesian blocks can be applied to photon counts of binned light curves and even to individual photon count arrival times, thus not requiring a pre-defined binning. However, as Figure 1 illustrates, the eROSITA photon counts are highly variable as the source runs through the field-of-view in the survey scan, simply because of angle-dependent instrument sensitivity. For astrophysical inference, we are interested in source variability, rather than observation-induced variability. The Bayesian blocks algorithm could be extended with a new likelihood to incorporate this information. However, a further difficulty is that the background is not negligible for most sources. Some of its components are variable over time, especially those passing through the mirrors and those sensitive to spacecraft orientation relative to the sun. Others, such as the particle background, are persistent, and become dominant at large off-axis angles. An extension of Bayesian blocks to analyse source and background region light curve simultaneously would be desirable, building on the foundations outlined above. However, this is beyond the scope of this work. Therefore, we resort to the classic source rate and uncertainty estimators $\hat{R}(t)$ and $\hat{\sigma}(R)(t)$, which are corrected for the fractional exposure, and use the Gaussian Bayesian blocks implementation from astropy (Astropy Collaboration et al. 2013, 2018). This however requires pre-binned light curves.

In our application to binned light curves, all borders between time bins with observations are candidates for change points. Bayesian blocks begins with the hypothesis that the count rate is constant. For each candidate change point, it tries the hypothesis that the count rate is constant to some value before the change point, and constant to some value after the change point. The two hypothesis probabilities are compared using Bayesian model comparison. If the model comparison favours the split, each segment is analysed with the same procedure recursively. Finally, Bayesian blocks returns a segmented light curve, and

estimates for the count rate in each segment with its uncertainties.

The Bayesian model comparison requires a prior on the expected number of change points n_{cp} . We adopt the prior favoured by simulations of Scargle et al. (2013), $P(n_{\text{cp}}) = 4 - 73.53p_0n_{\text{cp}}^{-0.478}$ with the desired false positive rate set to $p_0 = 0.003$ (corresponding to 3σ). Variability is significantly “detected” by the Bayesian blocks algorithm when it identified at least one change point. We refer to n_{cp} as NBBLOCKS.

3.3.3. Fractional and Excess variance

A Poisson process is expected to induce stochasticity into the measurement. Excess variance methods (Edelson et al. 1990; Nandra et al. 1997; Edelson et al. 2002; Vaughan et al. 2003; Ponti et al. 2014) quantify whether the observed stochasticity shows additional variance, i.e., is over-dispersed.

Across bins, the mean net source count rate \bar{R}_S is:

$$\bar{R}_S = \frac{1}{N} \sum_i^N \hat{R}_S(t_i) \quad (10)$$

The observed variance of the net source count rates \hat{R}_S (one in each time bin) is:

$$\sigma_{\text{obs}}^2 = \frac{1}{N-1} \sum_i^N \left(\hat{R}_S(t_i) - \bar{R}_S \right)^2 \quad (11)$$

The Poisson noise expectation is computed with the mean square error computed from the error bars:

$$\overline{\sigma_{\text{err}}^2} = \frac{1}{N} \sum_i^N (\hat{\sigma}(R_S)(t_i))^2 \quad (12)$$

Subtracting off this expectation, we obtain the excess variance:

$$\sigma_{\text{XS}}^2 = \sigma_{\text{obs}}^2 - \overline{\sigma_{\text{err}}^2} \quad (13)$$

Normalising to the mean count rate, gives the normalised excess variance (NEV):

$$\text{NEV} = \frac{\sigma_{\text{XS}}^2}{\bar{R}_S^2} \quad (14)$$

The variable fraction of the signal, F_{var} , also known as the fractional root-mean-square (RMS) amplitude, is then defined as:

$$F_{\text{var}} = \sqrt{\text{NEV}} \quad (15)$$

The excess variance σ_{XS}^2 quantifies the over-dispersion, without making assumptions about the process causing the variability. Values of σ_{XS}^2 can however also become negative by chance, or when the measurement uncertainties are over-estimated. To avoid this problem (which affects F_{var}), we force NEV to not go below a small positive value (0.001).

Quantifying the significance of the excess variance is more difficult (Nandra et al. 1997). (Vaughan et al. 2003) used simulations to find the empirical formulas

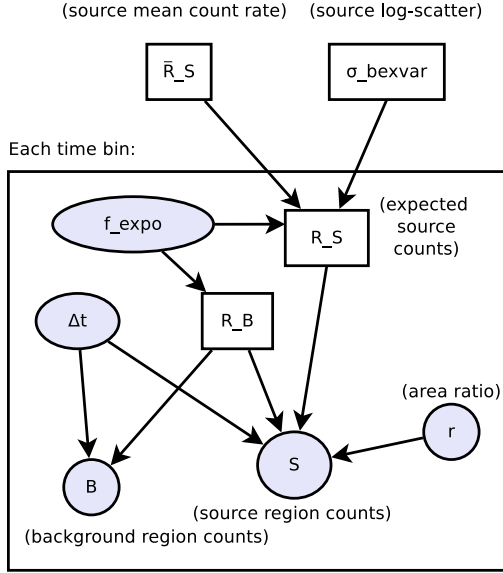


Fig. 7. Graphical model of the Bayesian excess variance method. Shaded circles indicate known values, related to the experiment setup or observed data. Rectangles indicate unknown parameters, including the unknown source count rate and the count rate in each time bin. An arrow from A to B indicates that the generation of B was influenced by A.

(valid for N from 2 to 2000 and F_{var} from 0 to 40%) for the uncertainty in the NEV and F_{var} estimators:

$$\sigma(\text{NEV}) = \sqrt{\frac{2}{N} \left(\frac{\sigma_{\text{err}}^2}{\bar{R}_S^2} \right)^2 + \frac{\sigma_{\text{err}}^2}{N} \times \left(\frac{2 \times F_{\text{var}}}{\bar{R}_S} \right)^2} \quad (16)$$

$$\sigma(F_{\text{var}}) = \frac{\sigma(\text{NEV})}{2 \times F_{\text{var}}} \quad (17)$$

The significance of the excess variance can then be defined as $\text{FVAR_SIG} = F_{\text{var}}/\sigma(F_{\text{var}})$ and $\text{NEV_SIG} = \text{NEV}/\sigma(\text{NEV})$.

3.3.4. Bayesian excess variance (bexvar)

The excess variance computation above assumes symmetric, Gaussian error bars. This limitation can be relaxed by modelling the entire data generating process. Towards this, we assume that at any time bin i , the rate $R_S(t_i)$ is distributed according to a log-normal distribution with unknown parameters:

$$\log R_S(t_i) \sim \text{Normal}(\log \bar{R}_S, \sigma_{\text{bexvar}}) \quad (18)$$

In this formulation, we need to estimate the mean logarithmic net source count rate ($\log \bar{R}_S$), the intrinsic scatter σ_{bexvar} as well as the rates at each time bin $R_S(t_i)$, giving $N + 2$ parameters. Equation 18 defines a prior for each bin's source count rate. This is a hierarchical Bayesian model (HBM), combined with the equations 1 and 2 which define the probabilities in each time bin. Figure 7 illustrates the relation between all quantities as a graphical model.

Priors for \bar{R}_S and σ_{bexvar} also need to be chosen. Here, we simply use uninformative, wide flat priors:

$$\log \bar{R}_S \sim \text{Uniform}(-5, 5) \quad (19)$$

$$\log \sigma_{\text{bexvar}} \sim \text{Uniform}(-2, 2) \quad (20)$$

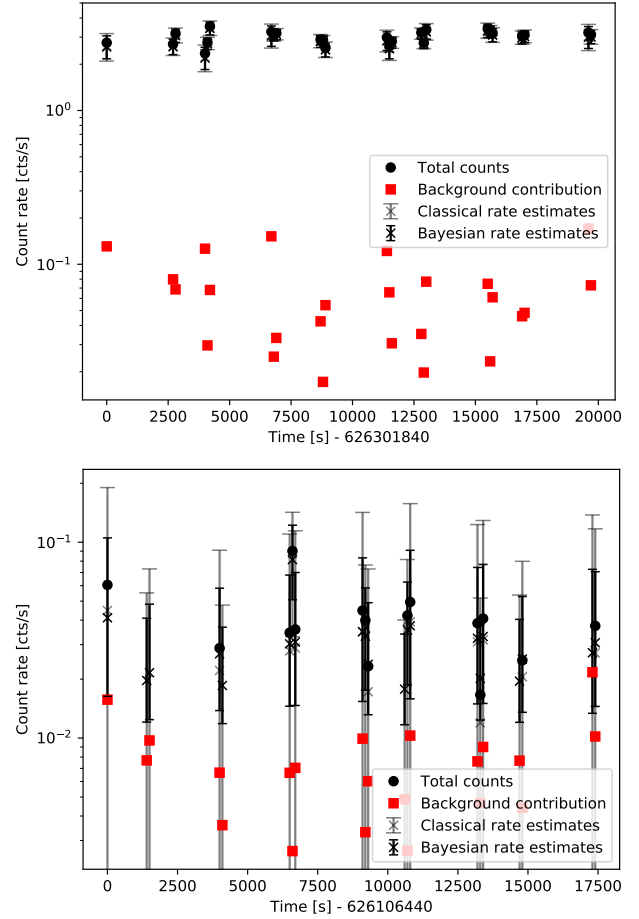


Fig. 8. Simulated light curves of *constant* sources with Poisson noise. Black circles show the total counts without background subtraction, red points show the expected background count rates in the source region (eq. 4). The *top panel* shows a high-count rate source with a constant 3 cts/s, where the source counts are always above the expected background counts. The *bottom panel* shows a low-count rate source with a constant 0.03 cts/s, where source region counts and background counts are comparable and show substantial Poisson scatter. Gray error bars show Classical net source count rate estimates (eq. 3 and 5). Black error bars show Bayesian net source count rate posterior distributions (eq. 7).

The mean count rate \bar{R}_S , has a straight-forward interpretation. In its posterior distribution, the Poisson uncertainty is directly incorporated.

Variability is quantified with σ_{bexvar} , which gives the intrinsic variance. This log-scatter on the log-count rate is a different quantity than the excess variance on the (linear) count rate, σ_{XS} . Because the variability is defined as a log-normal, this corresponds to the log-amplitude of a multiplicative process. The motivation for this is primarily of practical. Variable objects can be identified when the posterior distribution of σ_{bexvar} excludes low values. Here, we define SCATT_LO as the lower 10% quantile of the posterior, and use it as a variability indicator.

How can the above formulas be solved to actually produce probability distributions on, say, σ_{bexvar} ? The first step is the posterior probability computation. If we assume a source count rate $R_S(t_i)$ at each bin, eq. 2 indicates how to compute the Poisson probability to detect the source region counts S . The background

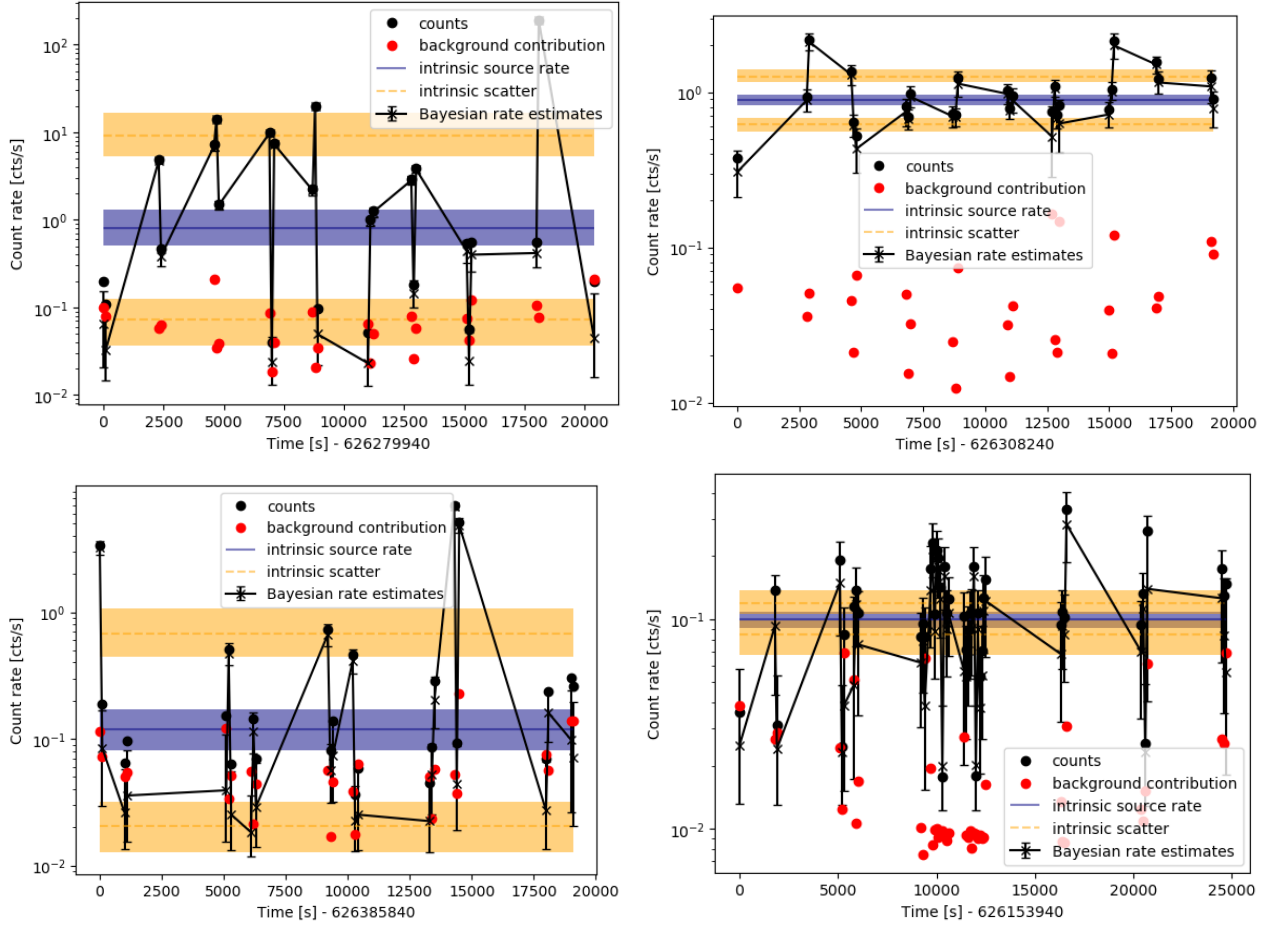


Fig. 9. As in Fig. 8, but for *gaussvar* sources. The intrinsic count rate is randomly varied following a log-normal distribution around a base-line count rate. Left panels show cases with $\sigma = 1\text{dex}$ variations, clearly visible in the scatter of the total counts (black points) in both bright (top panel) and faint (bottom panel) sources. Right panels show lower variations ($\sigma = 0.1\text{dex}$). In the bright case (top panel) the scatter of the black points is substantially larger than the error bars, while in the faint case (bottom) error bars overlap. In the top panel the background contribution (red points) is well below the total counts (black), while in the bottom panel, they are comparable. The blue solid line and band shows the posterior median and 1σ uncertainty of the intrinsic source count rate \hat{R} , computed using the *bexvar* method. The intrinsic scatter around the mean, σ_{bexvar} , is shown in orange dashed lines, indicating the upper and lower 1σ of the estimated log-Gaussian. The uncertainties on σ_{bexvar} are shown in orange bands. In all but the bottom right panel, the orange band is clearly separated from the blue band (indicating significant intrinsic variability).

count rate $R_B(t_i)$ also needs to be chosen and the Poisson probability to detect the background region counts B can be computed. If we further assume a value \bar{R}_S and σ_{bexvar} , eq. 18 computes the probability of the N chosen $R_S(t)$ values. Finally, eq. 19 and 20 specify the prior probability for \bar{R}_S and σ_{bexvar} , i.e., $\pi(\bar{R}_S)$ and $\pi(\sigma_{\text{bexvar}})$, respectively. To summarise, given the assumed $(2 \times N + 2)$ -dimensional parameter vector we compute $2N + 3$ probabilities for light curve data $D = (S_1, B_1, \dots, S_N, B_N)$:

$$\theta = (\bar{R}_S, \sigma_{\text{bexvar}}, R_S(t_1), \dots, R_S(t_N), R_B(t_1), \dots, R_B(t_N))$$

As we require all probabilities to hold simultaneously, we multiply them, obtaining the posterior probability function:

$$P(\theta|D) = \pi(\bar{R}_S) \times \pi(\sigma_{\text{bexvar}}) \times \prod_{i=1}^N P(R_S(t_i), R_B(t_i)|S_i, B_i) \quad (21)$$

where the per-bin posterior probability terms:

$$P(R_S(t_i), R_B(t_i)|S_i, B_i) = P(R_S(t_i)|\bar{R}_S, \sigma_{\text{bexvar}}) \times \pi(R_B(t_i)) = P(S_i, B_i|R_S(t_i), R_B(t_i)) \quad (22)$$

and the per-bin likelihoods being the product of equations 1 and 2:

$$P(S, B|R_S, R_B) = P(B|R_B) \times P(S|R_S, R_B) \quad (23)$$

We are now equipped with a posterior over a $(2 \times N + 2)$ -dimensional parameter space. To compute probability distributions for a parameter of interest, say, σ_{bexvar} , all other parameters need to be marginalised out:

$$P(\sigma_{\text{bexvar}}|D) = \int \int \int P(\theta|D) \times d\bar{R}_S dR(t_i) dR_B(t_i) \quad (24)$$

The exploration of the posterior probability distribution on σ_{bexvar} can be achieved with Markov Chain

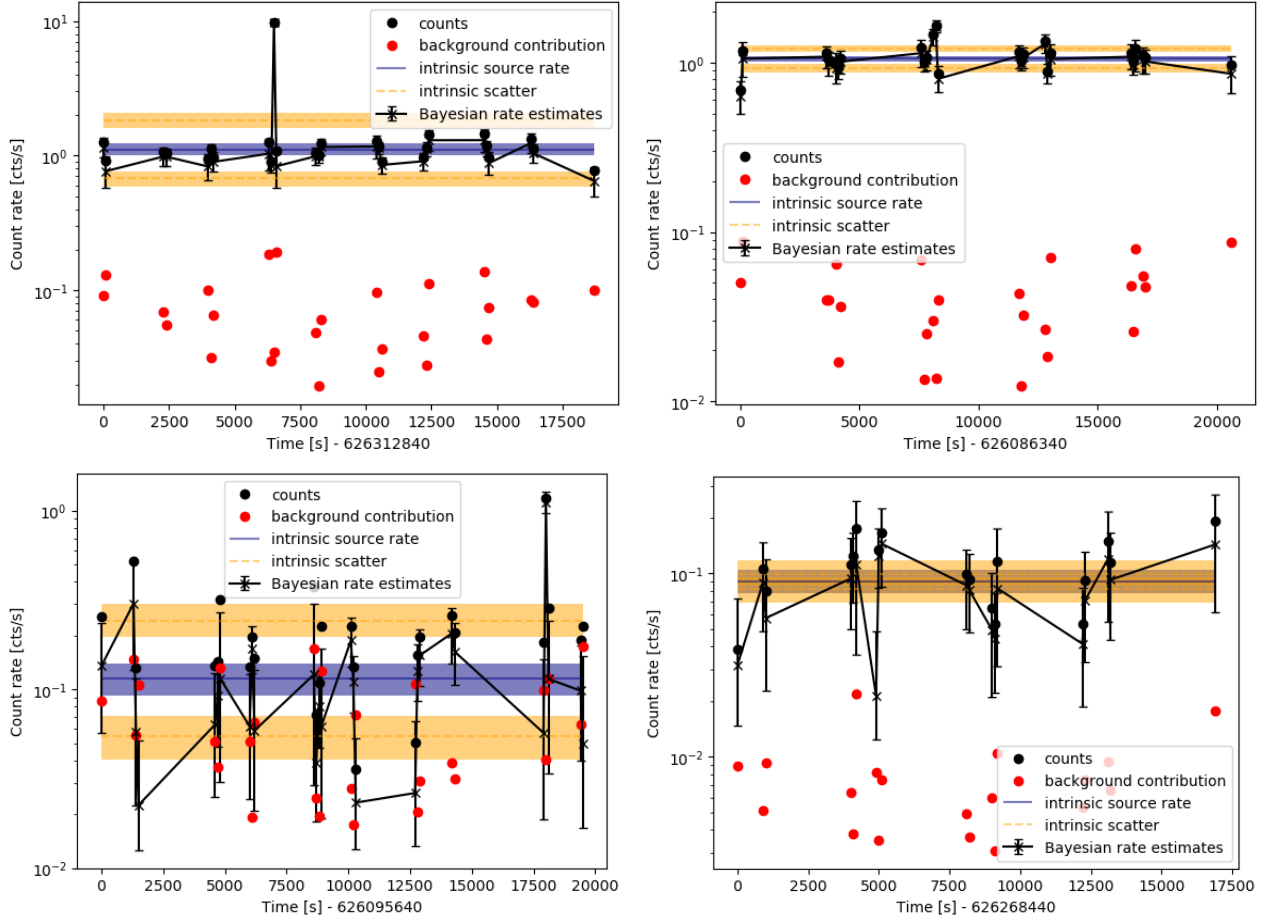


Fig. 10. As in Fig. 9, but for *flare* sources. One time bin has its count rate increased by a factor of k . Top (bottom) panels show bright (faint) source base-line count rates. Top panels show a flare of $k = 10$, bottom panels a $k = 2$ flare.

Monte Carlo algorithms. These repeatedly propose values θ , and sample the values of σ_{bexvar} proportional to their posterior probability. However, in practice, the convergence of this computation is slow and not always stable, even with state-of-the-art methods.

Substantial improvements are possible for rapid computation. Firstly, section 3.1.2 already derived the marginalised likelihood for the per-bin source rates $P(S, B | R_S)$. These can be represented as an array $P_{i,j}$ giving the probability for time bin i over a grid of source rates R_j . Using the normal distribution defined by \bar{R}_S and σ_{bexvar} , we can compute at each grid $R(t)$ value its probability, and marginalise over j over the grid for each time bin. Thus, we approximate eq. 21 with:

$$P(D | \bar{R}_S, \sigma_{\text{bexvar}}) \propto \prod_{i=1}^N \sum_{j=1}^M P_{i,j} \times \text{Normal}(\log R_j | \log \bar{R}_S, \sigma_{\text{bexvar}}) \quad (25)$$

We are now left with only a two-dimensional probability distribution. We employ the nested sampling Monte Carlo algorithm MLFriends (Buchner 2016, 2019) implemented in the UltraNest Python package² (Buchner 2021) to obtain the probability distribution $P(\sigma_{\text{bexvar}} | D)$ using the likelihood (eq. 25) and priors (eq. 19 and 20).

The probability distribution $P(\sigma_{\text{bexvar}} | D)$ quantifies the variability amplitude supported by the data. To illustrate the typical behaviour of this probability distribution, once a few data points are added, the highest values of σ_{bexvar} are excluded and receive a low probability. When inconsistent data points (excess variance) is present, also the lowest values of σ_{bexvar} receive a low probability, concentrating the probability distribution near the true value. Therefore, a conservative indicator of the magnitude of the excess variance is the lower 10% quantile of the distribution, which we term SCATT_LO. We adopt this single summary statistic for comparison with the other methods. Similar to the other methods (NEV, Bayesian blocks), the significance quantification needs to be obtained with simulations.

3.4. Method comparison

To summarise, we consider four methods (and their estimators):

- Amplitude Maximum Deviation (AMPL_MAX)
- Normalised Excess Variance (NEV)
- Bayesian Blocks (NBBLOCKS)
- Bayesian Excess Variance (SCATT_LO)

All of these methods rely on binned light curves. They are therefore sensitive to the chosen number of bins, which modulates how much information is contained in each bin. All methods neglect time information and are

² <https://johannesbuchner.github.io/UltraNest/>

oblivious to the order of measurements. The exception is Bayesian blocks. All methods disregard gaps.

To quantify the significance of a detection, the first three methods have already a significance indicator (AMPL_SIG, NEV_SIG, NBBLOCKS). However, these are derived under specific assumptions or simulation settings: The existing simulations of Vaughan et al. (2003) and (Scargle et al. 2013) did not consider the scenario with variable sensitivity and non-negligible backgrounds. The AMPL_SIG does not account for the number of data points, which increase the chance of getting a large AMPL_MAX by chance. The Bayesian blocks, NEV and AMPL_SIG methods adopt imperfect Gaussian approximations. Because of these limitations, simulations are necessary to detect variable objects with desired reliability characteristics. For these reasons, we verify that the significance indicators correspond to the desired p-values, for example, in constant sources NEV_SIG should exceed 3σ only in 0.1% of cases by chance. We prefer to verify NEV_SIG and AMPL_SIG rather than NEV and AMPL_MAX, as the existing formulae already largely correct for trends with size of the uncertainties and the number of data points. In Bayesian blocks, unjustified change points should also rarely introduced by chance.

3.5. Simulation setup

To calibrate the significance threshold at which an object is classified as variable, we use extensive simulations. Four datasets are generated. Each data set is created based on the 27910 eFEDS light curves, taking their time sampling (ΔT) and f_{expo} values as is. This generates a data set under identical conditions. We do not vary the vignetting and other corrections, i.e., assume that the instrument model is correct. Background counts are sampled using equation 1 with Poisson random numbers assuming the measured, time-average \hat{R}_B as a constant across all time bins for that source. Source counts are sampled using equation 2 with Poisson random numbers, using the sum of the scaled background rate and the desired source rate $R(t)$ at that time step. For reasonable ranges of $R(t)$, recall that the typical number of counts in a 100 s bin is below 10 for most sources and time bins, but can reach up to a few hundreds (see Fig. 4 and Boller et al. 2021). We therefore consider count rate ranges between $\mu = 0.03$ cts/s and 3 cts/s.

For the source rate, four scenarios are considered:

1. *constant*: The count rate are constant: $R(t) = \mu$. The sample is divided into five equally sized groups. Each group is assigned a different count rate (0.03, 0.1, 0.3, 1 and 3 cts/s). Figure 8 presents two examples of *constant* light curves, showing the lowest and highest count rates considered. The Poisson scatter is strongly noticeable.
2. *gaussvar*: For each time bin, a count rate is drawn independently from a log-normal distribution with mean $\log \mu$ and variance σ : $\log R(t) \sim \text{Normal}(\log \mu, \sigma)$. The sample is divided into five equally sized groups. Each group is assigned a different mean count rate ($\mu = 0.03, 0.1, 0.3, 1$ and 3 cts/s). The groups are further subdivided into five subgroups. Each subgroup is assigned a different variance ($\sigma = 0.03, 0.1, 0.3, 0.5, 1.0$). This represents the behaviour of long-term revisits of AGN

(e.g., Maughan & Reiprich 2019). Figure 9 presents four examples of *gaussvar* light curves, varying the intrinsic count rates (left vs. right panels) and the strength of the intrinsic scatter (top vs. bottom panels). These examples also illustrate the inference of *bexvar*, estimating the mean, intrinsic count rate (blue line), its uncertainty (blue band), the count rate log variation (orange lines) and its uncertainty (orange bands).

3. *flare*: Same as *constant*, but in one randomly selected time bin the count rate is increased by a factor k . The groups are subdivided into subgroups. Each subgroup is assigned a different factor ($k = 30, 10, 5, 2, 1.5, 1.3$). The subgroups with $k = 30$ and 5 are half as large as the other subgroups. Figure 10 presents four examples of *flare* light curves, varying the intrinsic count rates (left vs. right panels) and the flare strength k (top vs. bottom panels). Weak flares become difficult to notice in the presence of Poisson noise.
4. *redvar*: To complement the white noise process in *gaussvar*, a correlated random walk (red noise) is also tested. Specifically, we adopt a first-order Ornstein-Uhlenbeck process $x_{i+1} = \phi \times x_i + \Delta t \times \text{Normal}(0, 1)$. This generates on short time-scales a powerlaw power spectrum with index -2, not atypical of AGN (e.g., Simm et al. 2016). To always be near this regime, we choose a long dampening time-scale $T = 100,000$ s, so that $\phi = \exp(-\Delta t/T)$ is close to 1. The long-term variance of this random walk is $\sigma^2 = \Delta t^2/(1 - \phi^2)$. Following Vaughan et al. (2003), time bins are super-sampled forty-fold to avoid red noise leaks, and then summed. Finally, the random walk is normalised and mixed as a variable fraction f_{var} with a constant to obtain the source count rate as $R(t_i) = \mu \times (1 + f_{\text{var}} \times x_i/\sigma)$. The mean μ is varied in groups as in *gaussvar*, and five equally sized subgroups set f_{var} to 0.03, 0.1, 0.2, 0.3 and 0.5, motivated by the range observed in X-ray binaries (Heil et al. 2015).

Simulating other types of variability, such as exponential or linear declines, sinusoidal variations are outside the scope of this work. However, because almost all methods adopted here ignore the order of measurements, they are covered to some degree by the *gaussvar* setup.

To achieve accurate quantification of the methods, many simulations are needed. In total, 27908 *constant* simulations (all eFEDS sources are used as templates), 14003 *gaussvar* simulations (eFEDS sources with even IDs are templates), 13905 *flare* simulations (eFEDS sources with odd IDs are templates) and 14003 *redvar* simulations (same as *gaussvar*) were generated for the soft band. A similar number of simulations was performed for the hard band, except 28 light curves have no valid time bins and were discarded. We primarily focus on the soft band simulations.

4. Results

4.1. Thresholds for low false positive rates

To find a reliable threshold corresponding to a low false positive rate, the *constant* data set is used. The idea is

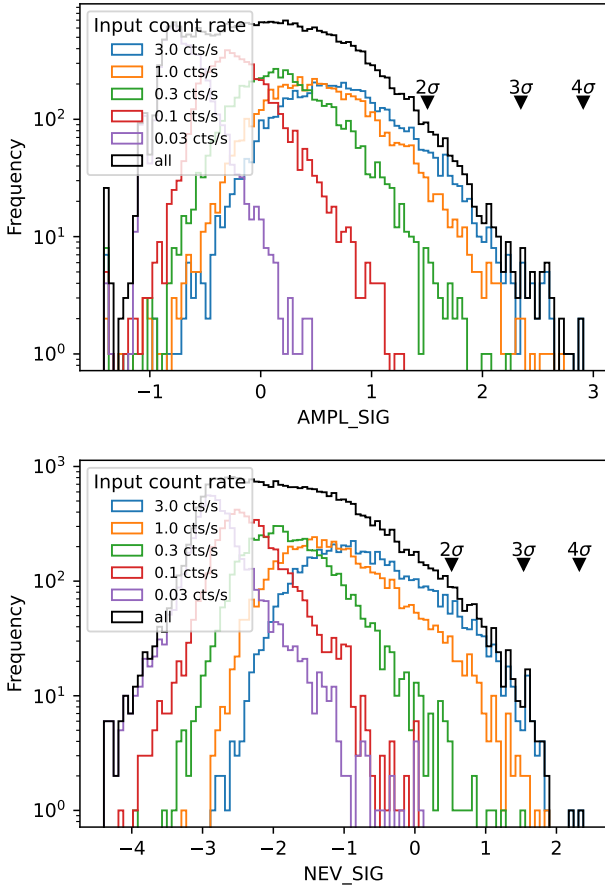


Fig. 11. Estimator distribution for simulated *constant* light curves. *Top panel:* amplitude maximum deviation significance (eq. 9). *Bottom panel:* Significance of the excess variance and variability fraction (eq. 16). Each coloured histogram represents a set of simulations with the indicated constant input count rate. For the full data set (black histogram), black downwards triangles point to the 2σ , 3σ and 4σ equivalent quantiles of the distribution.

to choose a threshold that rarely triggers in this non-variable data set and that it corresponds to some desired p-value. For a given method, its variability estimator is computed for each simulated *constant* light curve. This gives an estimator distribution for non-variable sources. Figures 11 and 12 show the distributions for the estimators of the maximum amplitude, excess variance, bexvar and Bayesian blocks methods at various input count rates. The expectation is that given that these are non-variable sources, a significance value as extreme as 3σ indeed occurs with a frequency (p-value) corresponding to 0.27%. However, Figure 11 illustrates that the distribution of significance estimators (x-axis, in units of σ), does not exactly match the observed 2σ , 3σ , 4σ quantiles of the distribution. This is because the significance estimators employ approximations such as Gaussian errors. For example, the normalised excess variance under-estimates the significance: 1σ significances almost never occur in data sets with < 1 cts/s. The amplitude maximum deviation also appears to slightly underestimate the significance ($\text{AMPL_SIG} > 2$ is reached in fewer than 1% of cases). The deviations are most extreme in the low count rate regime, where AMPL_SIG and NEV_SIG values never exceed 1 by chance.

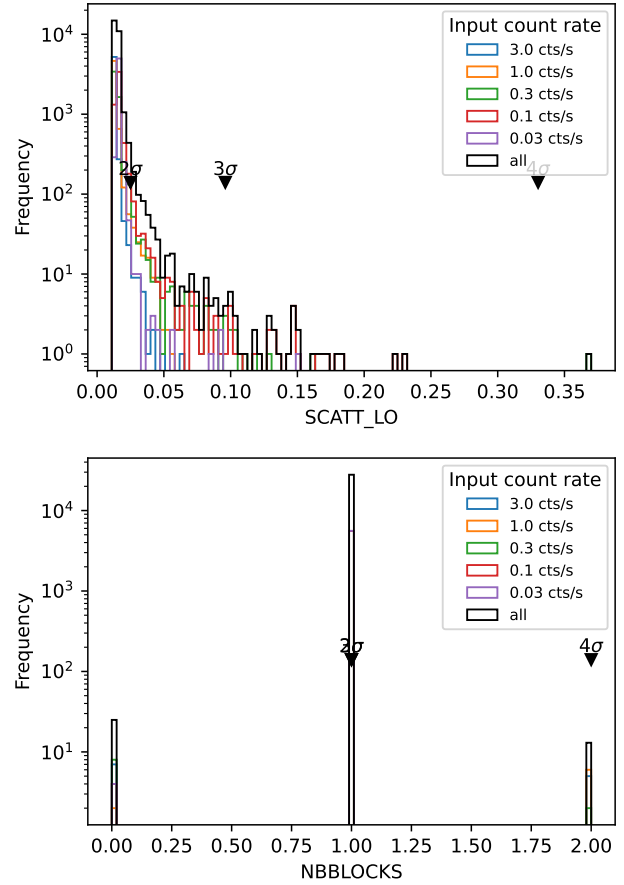


Fig. 12. As in Fig. 11, but for the bexvar SCATT_LO estimator (*top panel*), and the number of change points (NBBLOCKS) from the Bayesian blocks algorithm (*bottom panel*). In case of NBBLOCKS, the 3 sigma quantile is still within NBBLOCKS=1.

We choose the threshold at the 3σ equivalent quantile of the distributions from Figures 11 and 12. This corresponds to a 0.3% false positive rate at that count rate. This approach can be applied to any estimators, whether it indicates a significance (like AMPL_SIG and NEV_SIG) or an effect size (like SCATT_LO and NBBLOCKS). Figure 13 shows these thresholds as a function of count rate. For excess variance (top panel of Figure 13), and AMPL_SIG (middle panel) it lies in the $0 - 2\sigma$ range, and decreases towards low count rates. Recall that AMPL_MAX measures the distance between the lower error bar of the highest point and the upper error bar of the lowest point. When counts are low, the conservatively estimated error bars are large and mostly overlapping, giving very small or negative AMPL_MAX values. The significance further judges the distance by the error bars. This leads to AMPL_SIG decreasing with count rate and to low numbers. A similar effect occurs with NEV_SIG due to the overly conservative error bars (see §3.1.1).

For the Bayesian excess variance, the SCATT_LO threshold has a peak and does not rise towards the extreme count rates (bottom panel of Figure 13). The difference to AMPL_SIG and NEV_SIG may be because SCATT_LO measures an effect size, not a significance. For Bayesian blocks, the significance threshold (bottom panel of Figure 12) is always at $n_{\text{cp}} = 1$. That

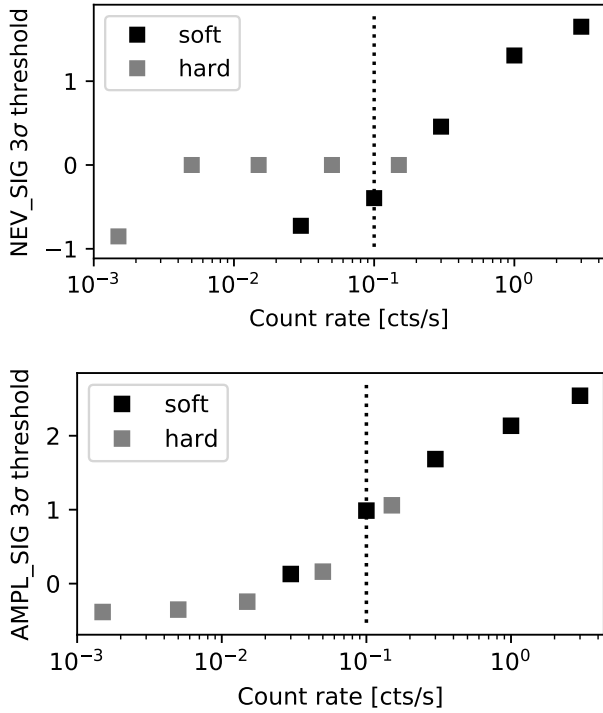


Fig. 13. Calibrated thresholds as a function of count rate. Points show 3σ extreme for each simulation, for excess variance (top), amplitude maximum deviation (middle panel) and Bayesian excess variance (bottom panel). The vertical dotted line indicates the typical uncertainty on \bar{R}_S .

Table 1. Reliable thresholds. Thresholds are calibrated to a 3σ false positive rate at all count rates. The expected number of false positives is derived assuming a count rate distribution.

Method	Threshold	Expected false positives
AMPL_SIG	2.6	0.1
NEV_SIG	1.7	0.1
FVAR_SIG	3.3	0.1
SCATT_LO	0.14	13.3

is, when the Bayesian block splits the light curve, it is reliable.

To derive a significance threshold for use in practice, a count rate distribution has to be assumed. Taking all simulations together would imply a log-uniform count rate distribution. In reality, the source count rates are peaking between 0.1 and 1 cts/s and decline towards the high end approximately like a powerlaw with index -1.5 . To be conservative, we choose the highest threshold across the simulated count rates, and present them in Table 1. Because the sample is dominated by faint sources, this leads to a lower false positive rate than 3σ (0.3%), and thus fewer than the naively expected number of false positives (75/27910). We estimate the expected false positive rate by weighing the simulations by a count rate powerlaw $\bar{R}_S^{-1.5}$. Table 1 lists the expected number of false positives in eFEDS for each method. For the Bayesian excess variance, the expected number is a dozen, for the other methods essentially no outliers are expected.

With the significance threshold chosen, we can now test which method is most sensitive to detect variability.

4.2. Sensitivity evaluation

The goal of this section is to identify the right variability method for detecting each type of variability. While the different methods are based on the same data (binned light curves), they vary in assumptions and how they use this information. Some ignore the order, some ignore all but the most extreme points.

We quantify the sensitivity of each method using the *gaussvar*, *redvar* and *flare* data sets. To do so, we apply the methods to each simulated light curve and compute the fraction above the significance thresholds calibrated in the previous section. This fraction is the completeness of the method. The simulations vary input count rate, strength and type of variability, allowing an in-depth look at the behaviour of the different methods. This allows us to characterise the detection efficiency by type (Figure 14 for *flare*, Figure 15 for *gaussvar*, Figure 16 for *redvar*), but also down to which k and σ values variability the methods are sensitive.

For flares (Figure 14), amplitude maximum deviation and Bayesian excess variance are the most sensitive method. The amplitude maximum deviation performs better at very high count rates, while the Bayesian excess variance is most complete in all other situations. Flares of a factor of 5-10 are detectable for typical eROSITA sources with these methods. The normalised excess variance has comparable completeness as the Bayesian excess variance, except at the lowest count rates. Bayesian blocks is less efficient at all count rates.

For white noise source variability from a log-normal distribution (Figure 15), the Bayesian excess variance is the most sensitive method at all count rates, followed by the normalised excess variance, amplitude maximum deviation and Bayesian blocks. In the more realistic red noise scenario with a small variable fraction (Figure 16), Bayesian excess variance also performs best in all but one simulation subgroup. Here, however, the Bayesian block algorithm performs similarly well. Overall, only large fractional variances ($f_{\text{var}} \geq 30\%$) in the high count-rate sources ($\bar{R}_S > 1 \text{ cts/s}$) can be detected. To compare Figure 15 and 16, $\sigma \approx f_{\text{var}}/2$, if the random walk is well sampled.

5. Discussion and Conclusion

This work focused on characterizing four methods for detecting source variable X-ray sources: the amplitude maximum deviation and Bayesian excess variance, normalised excess variance and Bayesian blocks.

5.1. Bexvar

The Bayesian excess variance (bexvar) is presented here for the first time. It is a fully Poissonian way to quantify source variability in the presence of background. We publish the bexvar code as free and open source Python software at <https://gitlab.mpcdf.mpg.de/jbuchner/bexvar>.

Currently, a simple time-independent log-normal distribution is assumed. However, the hierarchical Bayesian model is extensible. More complex variability models, such as fitting linear, exponentially declining, or periodic (sinusoidal) signals and potentially autoregressive moving average processes (see e.g., Kelly

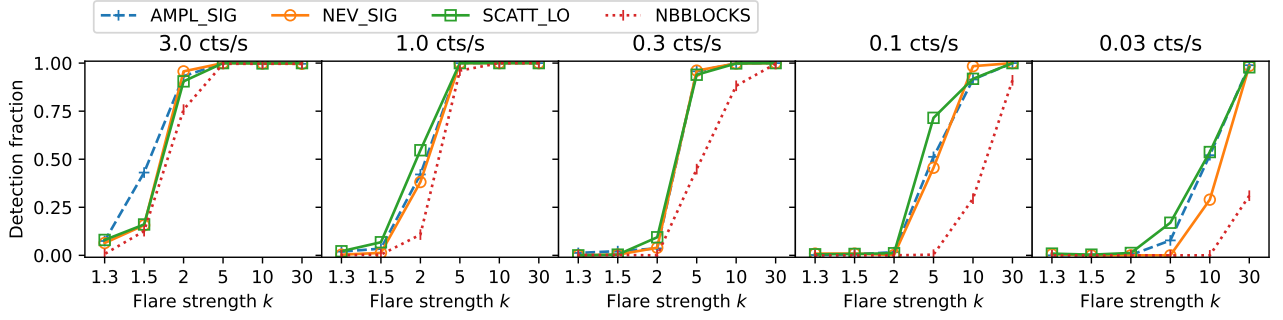


Fig. 14. Sensitivity of methods to detecting flares. Panels represent simulations with increasing input count rates from left to right. Flares of varying strengths are injected (x-axis). The fraction of objects where the method gives an estimate above the significance threshold is shown in the y-axis. At very high counts (left panels), the AMPL_SIG has the highest fraction. At medium and low counts, SCATT_LO has the highest detection fraction overall.

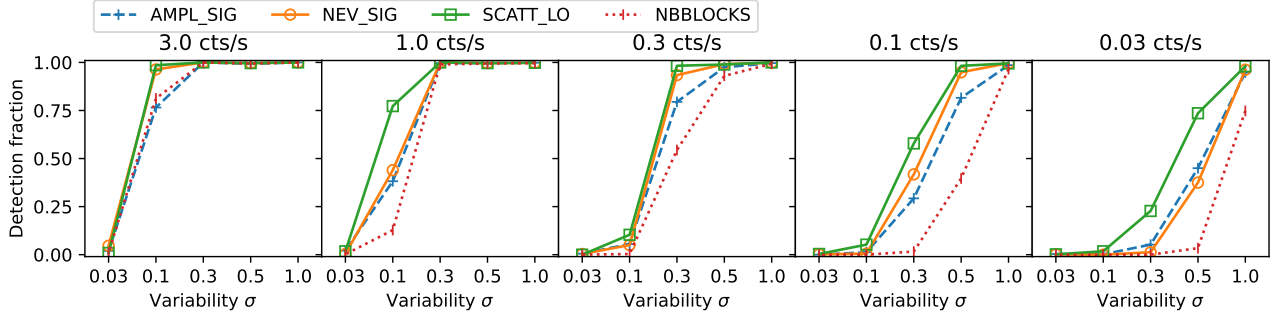


Fig. 15. As in Fig. 14, but for simulated white log-normal variability of varying strength σ (in dex). SCATT_LO has the highest detection fraction overall.

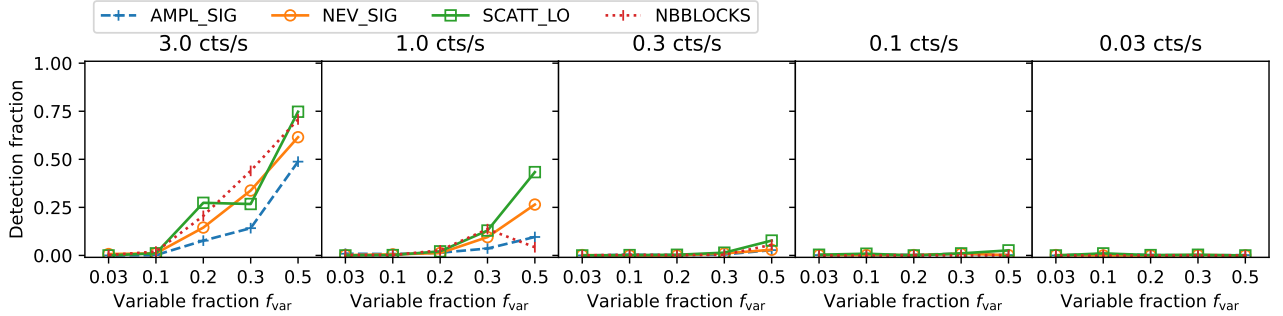


Fig. 16. As in Fig. 14, but for simulated red-noise variability of varying fraction f_{var} . Bayesian blocks has the highest detection fraction across all panels.

et al. 2014) can be implemented and applied to Poisson data.

Employing the Bayesian excess variance as a method to detect variability has some limitations. Requiring the 10% quantile on the log-normal scatter to exceed 0.14 dex makes a cut on significance and effect size. This will not detect barely variable sources even when the data are excellent. Bayesian model comparison of a constant model to a log-normal model may be even more powerful discriminator. Indeed, the strength of the Bayesian excess variance is not in the detection of variability, but in variability quantification. In appendix A, we verify that the input parameters can be accurately and reliably retrieved.

5.2. Efficient detection of variable sources for eROSITA

When comparing the four methods, we find that each method has strengths in detecting certain types of variability. For flares, amplitude maximum deviation is both sensitive and simple to compute. It is optimized to detect single outliers, so it is not surprising that it performs well here. However, it is perhaps somewhat surprising that Bayesian excess variance performs similarly well. This may be because it models the Poisson variations carefully, and is sensitive to excess variance. Both methods outperform the normalised excess variance and Bayesian blocks. We presume that carefully modelling the Poisson (source and background) noise leads to Bayesian excess variance outperforming the classical normalised excess variance.

For intrinsic log-normal variability, the Bayesian excess variance performs best overall. Comparing across panels in Figure 15, it allows detecting vari-

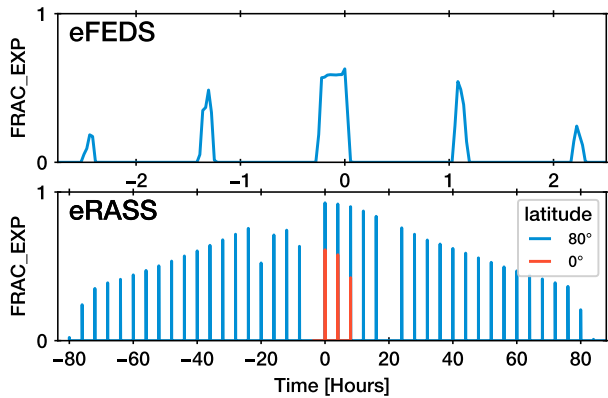


Fig. 17. Fractional exposure for an arbitrary eFEDS source (top panel) and two eRASS source at different ecliptic latitudes (bottom panel).

ability in sources three times fainter than Bayesian blocks with Gaussian noise. This is expected, because it models the chosen simulated white noise process. At low count rates, it substantially outperforms the normalised excess variance, which assumes the same model but uses Gaussian approximations. It is surprising that amplitude maximum deviation also outperforms the normalised excess variance, even though the latter considers all points. However, the trends change when white noise is replaced with a more realistic red noise. In that case, because data points are correlated in time, the order becomes important. Bayesian blocks, the only method tested here that takes the order of data points into account, performs better in this case. However, the detection efficiencies for realistic source parameters are very modest for all methods.

For observing patterns yielding only few (< 20) light curve data points, amplitude maximum deviation and Bayesian blocks are quick but effective methods, and therefore recommended for large surveys. The Bayesian excess variance requires more computational resources, but identifies a larger number of variable sources, especially in the low-count regime. This is demonstrated by our simulations but also true in practice. All four presented methods are applied to the eFEDS observations in Boller et al. (2021), at the same false positive rate (0.3%). The 65 sources significantly detected by one of the four methods, primarily consist of flaring stars and variable active galactic nuclei. All methods were able to detect variability among the 2% brightest sources of the eFEDS sample. However, the Bayesian excess variance more than doubled the number of sources, and detects variability down to source count rates which encompass 20% of the eFEDS sample.

5.3. Outlook for the eROSITA all-sky survey

In some regards, the eFEDS survey investigated here has similar properties to the eROSITA all-sky survey (eRASS). eRASS will ultimately consist of eight all-sky scan. These scans take six months to complete. With exception of sources near the ecliptic poles, which require different treatment (blue in Figure 17), most sources are visited over a period of a few days, and covered repeatedly for a few minutes (orange in Figure 17). This cadence pattern (3-8 chunks of obser-

vations, each resolved into multiple time bins) is not unlike the eFEDS light curve cadence. The total exposure time of eFEDS is designed to be comparable to that of eRASS. Therefore, sources of similar count distributions are expected. Thus the simulation setup to test and compare variability methods, as well as the derived significance thresholds, have applicability also to the final eRASS observations.

In conclusion, we recommend the Bayesian excess variance and amplitude maximum deviation methods for the detection of variable sources in eROSITA, with the significance thresholds specified in Table 1. However, variability detection and characterization methods benefit past, present and future high-energy experiments. Improvements in methodology can lead to new discoveries in archival data and allow future mission such as Athena (Nandra et al. 2013) and Einstein Probe (Yuan et al. 2015) to deliver more events in real time.

6. Software packages

matplotlib (Hunter 2007), UltraNest³ (Buchner 2021), astropy⁴ (Astropy Collaboration et al. 2013, 2018), gammapy⁵ (Deil et al. 2017; Nigro et al. 2019).

Acknowledgements. We thank the anonymous referee for insightful comments that improved the paper. JB thanks Mirko Krumpe for comments on the manuscript. This work is based on data from eROSITA, the soft X-ray instrument aboard SRG, a joint Russian-German science mission supported by the Russian Space Agency (Roskosmos), in the interests of the Russian Academy of Sciences represented by its Space Research Institute (IKI), and the Deutsches Zentrum für Luft- und Raumfahrt (DLR). The SRG spacecraft was built by Lavochkin Association (NPOL) and its subcontractors, and is operated by NPOL with support from the Max Planck Institute for Extraterrestrial Physics (MPE). The development and construction of the eROSITA X-ray instrument was led by MPE, with contributions from the Dr. Karl Remeis Observatory Bamberg & ECAP (FAU Erlangen-Nuernberg), the University of Hamburg Observatory, the Leibniz Institute for Astrophysics Potsdam (AIP), and the Institute for Astronomy and Astrophysics of the University of Tübingen, with the support of DLR and the Max Planck Society. The Argelander Institute for Astronomy of the University of Bonn and the Ludwig Maximilians Universität Munich also participated in the science preparation for eROSITA. The eROSITA data shown here were processed using the eSASS/NRTA software system developed by the German eROSITA consortium.

Appendix A: Parameter Recovery

While the focus of this work is on the detection of variability, some of the methods employed quantify the variability. This depends on the assumed variability model, which are for example step functions in Bayesian blocks and (log) normal count rate scatter for the (Bayesian) excess variance. Based on the flare and white noise simulations, the recovery of methods that closely resemble these signals are investigated.

Figure A.1 compares the injected log-variance to the inferred Bayesian excess variance in the *gaussvar* simulations. At all count rates and variability levels, the injected variance is correctly recovered.

Figure A.2 compares the injected flare amplitude to the *ampl_max* measure. The distribution of values is

³ <https://johannesbuchner.github.io/UltraNest/>

⁴ <https://www.astropy.org/>

⁵ <https://gammapy.org/>

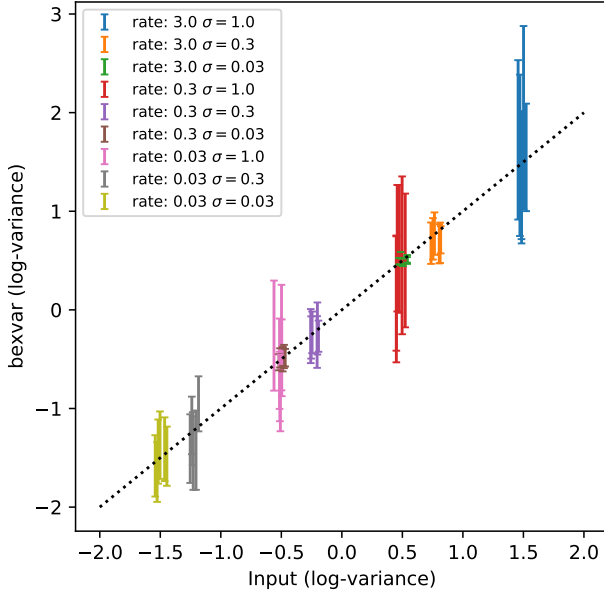


Fig. A.1. Inferred Bayesian excess variance for various simulated variances and count rates. Error bars indicate the 95% credible interval for an arbitrary subset of the simulations. A small displacement in the x-axis is added to each data point for clarity. The dotted line indicates the 1:1 correspondence.

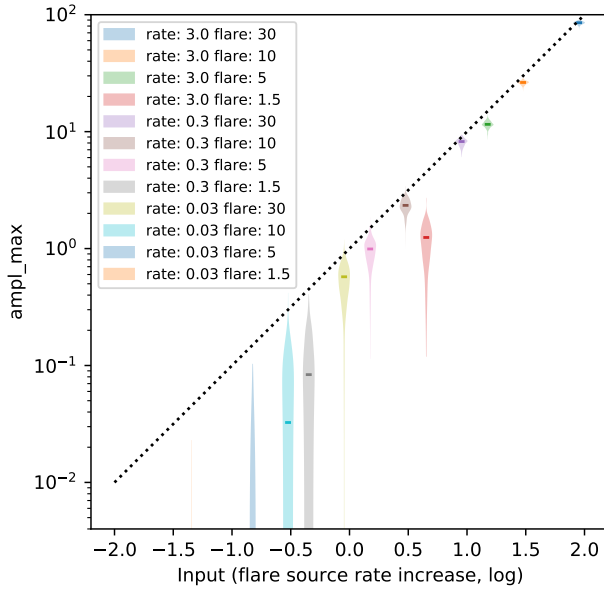


Fig. A.2. Inferred amplitude maximum deviation distribution (violin plots) for various input flare strengths. The dotted line indicates the 1:1 correspondence. Most `ampl_max` values typically lie below this line.

indicated as a violin plot. Recall that `ampl_max` measures the span between error bars, and thus tends to conservatively under-estimate the flare strength. Nevertheless, there is good overall correspondence.

References

Armstrong, D. J., Kirk, J., Lam, K. W. F., et al. 2016, *MNRAS*, 456, 2260
 Astropy Collaboration, Price-Whelan, A. M., Sipőcz, B. M., et al. 2018, *AJ*, 156, 123
 Astropy Collaboration, Robitaille, T. P., Tollerud, E. J., et al. 2013, *A&A*, 558, A33

Bachetti, M., Harrison, F. A., Walton, D. J., et al. 2014, *Nature*, 514, 202
 Barlow, R. 2003, in *Statistical Problems in Particle Physics, Astrophysics, and Cosmology*, ed. L. Lyons, R. Mount, & R. Reitmeier, 250
 Boller, T., Freyberg, M. J., Trümper, J., et al. 2016, *A&A*, 588, A103
 Boller, T., Schmitt, J. H. M. M., Buchner, J., et al. 2021, *arXiv e-prints*, arXiv:2106.14523
 Brunner, H., Liu, T., Lamer, G., et al. 2021, *arXiv e-prints*, arXiv:2106.14517
 Buchner, J. 2016, *Statistics and Computing*, 26, 383
 Buchner, J. 2019, *PASP*, 131, 108005
 Buchner, J. 2021, *The Journal of Open Source Software*, 6, 3001
 Cameron, E. 2011, *PASA*, 28, 128
 De Luca, A., Salvaterra, R., Belfiore, A., et al. 2021, *A&A*, 650, A167
 Debosscher, J., Sarro, L. M., Aerts, C., et al. 2007, *A&A*, 475, 1159
 Deil, C., Zanin, R., Lefaucheur, J., et al. 2017, in *International Cosmic Ray Conference*, Vol. 301, 35th International Cosmic Ray Conference (ICRC2017), 766
 Ducci, L., Ji, L., Haberl, F., et al. 2020, *SRG/eROSITA discovery of a bright supersoft X-ray emission from the classical nova AT 2018bej in the Large Magellanic Cloud*
 Edelson, R., Turner, T. J., Pounds, K., et al. 2002, *ApJ*, 568, 610
 Edelson, R. A., Krolik, J. H., & Pike, G. F. 1990, *ApJ*, 359, 86
 Gehrels, N. 1986, *ApJ*, 303, 336
 Gehrels, N., Chincarini, G., Giommi, P., et al. 2004, *ApJ*, 611, 1005
 Gehrels, N. & Mészáros, P. 2012, *Science*, 337, 932
 Heil, L. M., Uttley, P., & Klein-Wolt, M. 2015, *MNRAS*, 448, 3348
 Heinze, A. N., Tonry, J. L., Denneau, L., et al. 2018, *AJ*, 156, 241
 Holl, B., Audard, M., Nienartowicz, K., et al. 2018, *A&A*, 618, A30
 Hunter, J. D. 2007, *Computing In Science & Engineering*, 9, 90
 Jayasinghe, T., Stanek, K. Z., Kochanek, C. S., et al. 2019, *MNRAS*, 486, 1907
 Kelly, B. C., Becker, A. C., Sobolewska, M., Siemiginowska, A., & Uttley, P. 2014, *ApJ*, 788, 33
 Kim, D.-W., Protopapas, P., Byun, Y.-I., et al. 2011, *ApJ*, 735, 68
 Klebesadel, R. W., Strong, I. B., & Olson, R. A. 1973, *ApJ*, 182, L85
 Knoetig, M. L. 2014, *ApJ*, 790, 106
 Koenig, O., Wilms, J., Kreykenbohm, I., et al. 2020, *SRG/eROSITA detection of a bright flare of the millisecond pulsar PSR J1023+0038*
 Kraft, R. P., Burrows, D. N., & Nousek, J. A. 1991, *ApJ*, 374, 344
 Liu, J.-F., Bregman, J. N., Bai, Y., Justham, S., & Crowther, P. 2013, *Nature*, 503, 500
 Liu, T., Buchner, J., Nandra, K., et al. 2021, *arXiv e-prints*, arXiv:2106.14522
 Lorimer, D. R., Bailes, M., McLaughlin, M. A., Narkevic, D. J., & Crawford, F. 2007, *Science*, 318, 777
 Malyali, A., Rau, A., Merloni, A., et al. 2021, *A&A*, 647, A9
 Masci, F. J., Hoffman, D. I., Grillmair, C. J., & Cutri, R. M. 2014, *AJ*, 148, 21
 Matsuoka, M., Kawasaki, K., Ueno, S., et al. 2009, *PASJ*, 61, 999
 Maughan, B. J. & Reiprich, T. H. 2019, *The Open Journal of Astrophysics*, 2, 9
 Miniutti, G., Saxton, R. D., Giustini, M., et al. 2019, *Nature*, 573, 381
 Nandra, K., Barret, D., Barcons, X., et al. 2013, *ArXiv e-prints*
 Nandra, K., George, I. M., Mushotzky, R. F., Turner, T. J., & Yaqoob, T. 1997, *ApJ*, 476, 70
 Nigro, C., Deil, C., Zanin, R., et al. 2019, *A&A*, 625, A10
 Palaversa, L., Ivezić, Ž., Eyer, L., et al. 2013, *AJ*, 146, 101
 Petroff, E., Hessels, J. W. T., & Lorimer, D. R. 2019, *A&A Rev.*, 27, 4
 Ponti, G., Muñoz-Darias, T., & Fender, R. P. 2014, *MNRAS*, 444, 1829
 Predehl, P., Andritschke, R., Arefiev, V., et al. 2021, *A&A*, 647, A1
 Scargle, J. D., Norris, J. P., Jackson, B., & Chiang, J. 2013, *ApJ*, 764, 167
 Simm, T., Salvato, M., Saglia, R., et al. 2016, *A&A*, 585, A129

- Swank, J. H. 2006, *Advances in Space Research*, 38, 2959
- van Roestel, J., Duev, D. A., Mahabal, A. A., et al. 2021, *AJ*, 161, 267
- Vaughan, S., Edelson, R., Warwick, R. S., & Uttley, P. 2003, *MNRAS*, 345, 1271
- Weber, P. 2020, *GRB Coordinates Network*, 26988, 1
- Wilms, J., Kreykenbohm, I., Weber, P., et al. 2020, SRG/eROSITA detection of the bright, transient X-ray flare SRGt J123822.3-253206
- Yuan, W., Zhang, C., Feng, H., et al. 2015, *arXiv e-prints*, arXiv:1506.07735